Philosophical Magazine
Publication details, including instructions for authors and subscription information:
http://www.tandfonline.com/loi/tphm20

Phase-field simulations of magnetic field-induced strain in Ni_2MnGa ferromagnetic shape memory alloy

P.P. Wu [a b], X.Q. Ma [a], J.X. Zhang [b] & L.Q. Chen [b]

[a] Department of Physics, University of Science and Technology Beijing, Beijing 100083

[b] Department of Material Science and Engineering, Pennsylvania State University, University Park, PA 16802, USA

Available online: 11 Feb 2011

To cite this article: P.P. Wu, X.Q. Ma, J.X. Zhang & L.Q. Chen (2011): Phase-field simulations of magnetic field-induced strain in Ni_2MnGa ferromagnetic shape memory alloy, Philosophical Magazine, 91:16, 2102-2116

To link to this article: http://dx.doi.org/10.1080/14786435.2010.547527

Philosophical Magazine
Vol. 91, No. 16, 1 June 2011, 2102–2116

Taylor & Francis
Taylor & Francis Group

Phase-field simulations of magnetic field-induced strain in Ni_2MnGa ferromagnetic shape memory alloy

P.P. Wu[ab]*, X.Q. Ma[a], J.X. Zhang[b] and L.Q. Chen[b]

[a]*Department of Physics, University of Science and Technology Beijing, Beijing 100083;*
[b]*Department of Material Science and Engineering, Pennsylvania State University, University Park, PA 16802, USA*

(*Received 8 February 2010; final version received 8 December 2010*)

The magnetization and magnetic field-induced strain behavior of the ferromagnetic shape memory alloy, Ni_2MnGa, under constant compressive stress were studied using the phase-field method. Based on the evolving magnetic domain and martensitic structures, we analyzed the cycling effect, magnetization hysteresis, strain recoveries, and coupling between the domain wall and martensite twin boundaries. We compared the switching behavior of single variant and multivariant martensite structures. We observed three types of magnetic field-induced strain mechanisms, depending on the magnitude of the applied compressive stress. The study revealed that the martensite microstructure of the magnetic shape memory alloy plays an important role in magnetization and strain evolution during loading and unloading of an external magnetic field under different stress conditions. The results are compared with existing experimental observations.

Keywords: FSMA; MFIS; Ni_2MnGa; phase-field method

1. Introduction

Ferromagnetic shape memory alloys (FSMAs) have been the subject of extensive studies for more than two decades due to their multifunctional properties. They simultaneously exhibit ferromagnetism and ferroelasticity [1–16]. The mutual interactions among the ferromagnetic and ferroelastic order parameters, applied stress-fields and applied magnetic fields are complex and may result in a wide variety of interesting phenomena. For example, an external magnetic field may help recover the stress-induced strain [4], or a compressive stress field may lead to the recovery of the magnetic field-induced strain (MFIS) [6,7]. Furthermore, there is a strong correlation between the twin bands and magnetic domains, which leads to extremely large strains in FSMAs in response to magnetic fields [13,14]. The giant MFIS have a wide range of applications in sensors and actuators [15,16].

Ni_2MnGa is perhaps the most studied FSMA. Despite numerous investigations on its mechanical and magnetic properties, the mechanism for MFIS behavior is still not well understood. For example, it was demonstrated previously that MFIS occurs

*Corresponding author. Email: pingpingwu-ustb@126.com

ISSN 1478–6435 print/ISSN 1478–6443 online

DOI: 10.1080/14786435.2010.547527
http://www.informaworld.com

only once during a switching process and then the strain remains constant [2], i.e. the strain will not recover when the magnetic field decreases. However, it was suggested in 2003 by Heczko et al. [3] and Müllner et al. [4] that a compressive stress applied perpendicular to the direction of the applied magnetic field could lead to the recovery of the MFIS. Different magnetic hysteresis loops and different strain responses were also reported by Straka and Hezcko [5] and Hezcko [6] under various applied stress fields. Their studies show that, under a relatively low compressive stress of 1.4 MPa, fully recovered strain and magnetization were observed when the magnetic field decreases, leading to a double hysteresis magnetization loop and a butterfly-like stress–strain curve. However, under high compressive stress, the magnetic hysteresis displays a linear stress–strain relationship and only a small MFIS was observed. Furthermore, Karaca et al. [7,8] investigated the cycling effect and strain response under an incremental magnetic field in a single-variant martensite. They also schematically showed the magneto- and microstructure mechanisms for MFIS behavior.

To understand and predict the physical behavior of Ni_2MnGa under simultaneous action of magnetic and stress fields, there have been a number of theoretical studies on understanding the MFIS process. For example, Paul et al. [17,18] employed a simple geometrical model to show the crystalline region and model the dynamics of magnetization process with twin boundary motion. L'vov and co-workers [19,20] discussed the temperature dependence of magnetizations, stress–strain response and magnetically induced deformation through a phenomenological free energy model. Likhachev et al. [21] analyzed driving forces for the MFIS.

However, to fundamentally understand the physical nature of the MFIS requires knowledge of the evolving microstructures, including both the domain structure and martensitic microstructure [7,8]. Several numerical simulations have been conducted to study the microstructure evolution in FSMA [22–28].

In this paper, we study magnetic field-induced switching under a compressive stress by explicitly modeling the simultaneous magnetic domain and martensite twin structure evolution using the phase-field method. Coupling of the magnetic domain wall and the twin boundaries at different compressive stresses are analyzed to understand the origin of high MFIS. In particular, we investigated the demagnetization process, which was not considered in previous theoretical analyses. Our results will help to understand the so-called first-cycle effect [8] and the recovery strain in the switching process. To study the effect of martensite twin structure and obtain possibly higher MFIS, a single variant structure was simulated as a comparison to multi-variant cases. The obtained magnetization and strain curves are compared with existing experimental observations [5–8]. From differences in the magnetization hysteresis loop and strain curve under several applied compressive stresses, we classified the simulation results into three cases according to the magnitude of the applied compressive stress.

2. Free energy of FSMA

In our phase-field model, a given microstructure state of a ferromagnetic shape memory alloy is described by the local magnetization field $\boldsymbol{M}(r)$, which specifies the

magnetic domain structure, and a stress-free transformation strain field $\varepsilon^{o}_{ij}(r)$, which describes the martensitic microstructure.

The total free energy of a ferromagnetic shape memory alloy is

$$E = E_{\text{anis}} + E_{\text{exch}} + E_{\text{ms}} + E_{\text{external}} + E_{\text{Landau}} + E_{\text{gradient}} + E_{\text{me}} + E_{\text{elastic}}, \quad (1)$$

where E_{anis} is the magnetocrystalline anisotropy energy of a cubic crystal, given by

$$E_{\text{anis}} = \int \left[K_1\left(m_1^2m_2^2 + m_1^2m_3^2 + m_2^2m_3^2\right) + K_2m_1^2m_2^2m_3^2\right]\mathrm{d}V, \quad (2)$$

in which m_{i} are the components of the unit magnetization vector, $m = M/M_{\text{s}}$, M_{s} is the saturation magnetization, K_1 and K_2 are the anisotropy constants, and V is the volume.

E_{exch} in Equation (1) is the exchange energy related to the magnetization inhomogeneity and contributes to the magnetic domain wall energy:

$$E_{\text{exch}} = A\int (\text{grad}\,\boldsymbol{m})^2\mathrm{d}V, \quad (3)$$

where A is the exchange stiffness constant.

The magnetostatic energy, E_{ms} is written as

$$E_{\text{ms}} = -1/2\mu_0M_{\text{s}}\int \boldsymbol{H}_{\text{d}}\cdot\boldsymbol{m}\,\mathrm{d}V, \quad (4)$$

where μ_0 is the vacuum permeability, and $\boldsymbol{H}_{\text{d}}$ is the demagnetization field that arises from the long-range interactions among the magnetic moments in the system.

For a magnetic body in an external field, the Zeeman energy is given by

$$E_{\text{external}} = -\mu_0M_{\text{s}}\int \boldsymbol{H}_{\text{ex}}\cdot\boldsymbol{m}\,\mathrm{d}V, \quad (5)$$

where $\boldsymbol{H}_{\text{ex}}$ is the external applied magnetic field.

The Landau energy describing the martensitic transformation is written as

$$E_{\text{Landau}} = \int \left[Q_1e_1^2 + Q_2\left(e_2^2+e_3^2\right) + Q_3e_3\left(e_3^2-3e_2^2\right) + Q_4\left(e_2^2+e_3^2\right)^2 + Q_5\left(e_4^2+e_5^2+e_6^2\right)\right]\mathrm{d}V, \quad (6)$$

where Q_1, Q_2, and Q_5 are bulk, deviatoric and shear modulus, respectively. Q_3 and Q_4 denote third and fourth order elastic constants. e_{i} are the symmetry-adapted strain defined in term of the transformation strains [29], i.e.

$$\begin{aligned} e_1 &= (\varepsilon^0_{11} + \varepsilon^0_{22} + \varepsilon^0_{33})/\sqrt{3},\\ e_2 &= (\varepsilon^0_{11} - \varepsilon^0_{22})/\sqrt{2},\\ e_3 &= (2\varepsilon^0_{33} - \varepsilon^0_{11} - \varepsilon^0_{22})/\sqrt{6},\\ e_4 &= \varepsilon^0_{23},\\ e_5 &= \varepsilon^0_{13},\\ e_6 &= \varepsilon^0_{12}. \end{aligned} \quad (7)$$

E_{gradient} is the gradient energy, which is non-zero only at or around a twin boundary and introduced through the gradients of the order parameters.

$$E_{\text{gradient}} = \int \Big\{ 1/2g\Big[(\varepsilon^0_{11,1})^2 + (\varepsilon^0_{11,2})^2 + (\varepsilon^0_{11,3})^2 + (\varepsilon^0_{22,1})^2 + (\varepsilon^0_{22,2})^2 + (\varepsilon^0_{22,3})^2 + (\varepsilon^0_{33,1})^2 + (\varepsilon^0_{33,2})^2 + (\varepsilon^0_{33,3})^2\Big]\Big\} \mathrm{d}V, \tag{8}$$

where g is the strain gradient coefficient. The comma in a subscript stands for spatial differentiation; for example, $\varepsilon^0_{11,1}$ stands for $\partial\varepsilon^0_{11}/\partial x$.

The elastic energy E_{elastic} is given by

$$E_{\text{elastic}} = \int 1/2\ c_{ijkl}(\varepsilon_{ij} - \varepsilon^0_{ij})(\varepsilon_{kl} - \varepsilon^0_{kl})\mathrm{d}V, \tag{9}$$

where c_{ijkl} is the second order elastic stiffness tensor. ε_{ij} is the total strain.

The coupling effect between the magnetization and mechanical strain is very important for modeling the FSMA, which is described by the magnetoelastic coupling energy [30]. For a cubic crystalline magnetic material, it is written as

$$E_{\text{me}} = \int \left\{ B[\varepsilon^0_{11}(m_1^2 - 1/3) + \varepsilon^0_{22}(m_2^2 - 1/3) + \varepsilon^0_{33}(m_3^2 - 1/3)] \right\} \mathrm{d}V, \tag{10}$$

where B is the magnetoelastic coefficient, which is a measure of degree of coupling between strain and magnetization.

To obtain the strain field $\varepsilon^0_{ij}(r)$ distribution at a constant compression in FSMA, Khachaturyan's theory of microelasticity is employed to solve the mechanical equilibrium Equation (9). According to Khachaturyan's theory [31,32], the total strain can be separated into homogeneous and heterogeneous strains:

$$\varepsilon_{ij}(\mathrm{r}) = \overline{\varepsilon_{ij}} + \frac{1}{2}\left(\frac{\partial u_i(\mathrm{r})}{\partial r_j} + \frac{\partial u_j(\mathrm{r})}{\partial r_i}\right), \tag{11}$$

where the homogeneous strain $\overline{\varepsilon_{ij}}$ represents the macroscopic shape and volume change of a system. $u_i(r)$ is the ith component of the hetergeneous displacement. The heterogeneous strain is defined such that it does not change the macroscopic crystal shape or volume and satisfies the mechanical equilibrium equations:

$$\frac{\partial \sigma_{ij}}{\partial r_j} = 0, \tag{12}$$

where the σ_{ij} is the stress component and is defined by

$$\sigma_{ij} = c_{ijkl}\big(\varepsilon_{kl} - \varepsilon^0_{kl}\big). \tag{13}$$

Substituting Equations (11) and (13) into the equilibrium Equation (12) with the homogeneous modulus approximation, we have

$$c_{ijkl}\frac{\partial u_k}{\partial r_j \partial r_l} = c_{ijkl}\frac{\partial \varepsilon^0_{kl}}{\partial r_j}. \tag{14}$$

The displacement field $u_i(r)$ in Equation (14) is then solved in the reciprocal space through the Fourier transforms.

The homogeneous strain depends on the boundary condition. If a system is not allowed to deform, i.e. a clamped boundary condition, the homogeneous strain is zero

$$\overline{\varepsilon_{ij}} = 0. \tag{15}$$

When the system is subject to a homogeneous applied stress σ_{ij}^a, the total potential energy should take into account the mechanical loading contributions, i.e.

$$E_{\mathrm{p}} = E_{\mathrm{elastic}} - V\sigma_{ij}^a\overline{\varepsilon_{ij}}. \tag{16}$$

The homogeneous strain should be obtained by minimizing the total potential energy with respect to the homogeneous strain:

$$\frac{\partial E_p}{\partial \overline{\varepsilon_{ij}}} = \frac{\partial E_{\mathrm{elastic}}}{\partial \overline{\varepsilon_{ij}}} - \frac{V\sigma_{ij}^a\overline{\varepsilon_{ij}}}{\partial \overline{\varepsilon_{ij}}} = Vc_{ijkl}\overline{\varepsilon_{ij}} - c_{ijkl}\int \varepsilon_{kl}^0 \,\mathrm{d}V - V\sigma_{ij}^a = 0. \tag{17}$$

Therefore,

$$\overline{\varepsilon_{kl}} = \frac{1}{V}\int \varepsilon_{kl}^0 \,\mathrm{d}V + s_{ijkl}\sigma_{ij}^a, \tag{18}$$

where s_{ijkl} is the elastic compliance tensor. The total strain can be calculated using Equation (11); hence, the elastic energy can be obtained with Equation (9).

3. Field kinetic equations and simulation parameters

The temporal evolution of the magnetization distribution and, thus, the magnetic domain structure, is described by the Landau–Lifshitz–Gilbert (LLG) equation:

$$\left(1+\alpha^2\right)\frac{\partial M}{\partial t} = -\gamma_0 M \times H_{\mathrm{eff}} - \frac{\gamma_0\alpha}{M_s} M \times (M \times H_{\mathrm{eff}}), \tag{19}$$

where γ_0 is the gyromagnetic ratio, α is the damping constant, M_{s} is the saturation magnetization, and H_{eff} is the effective magnetic field:

$$H_{\mathrm{eff}} = -\frac{1}{\mu_0}\frac{\partial E}{\partial M}. \tag{20}$$

The martensitic microstructure distribution is described by the time-dependent Ginzburg–Landau (TDGL) equations:

$$\frac{\partial \varepsilon_{ii}^0(x,t)}{\partial t} = -L\frac{\delta E}{\delta \varepsilon_{ii}^0}, \tag{21}$$

where L is the kinetic coefficient related to twin boundary mobility.

The temporal evolution of the magnetic domain structure and the martensitic microstructure are obtained by simultaneously solving Equations (19) using the Gauss–Seidel projection method [33] and Equation (21) employing the semi-implicit Fourier-spectral method [34]. A model size of $256\Delta x \times 256\Delta y \times 1\Delta z$ are employed

for our 2D model, and periodic boundary conditions were applied along the x, y and z-axes. Here, Δx, Δy and Δz are grid spacing. The magnetic parameters can be found in [35,36]: $M_s = 6.02 \times 10^5\,\mathrm{A\,m^{-1}}$, $K_1 = 2.7 \times 10^3\,\mathrm{J\,m^{-3}}$, $K_2 = -6.1 \times 10^3\,\mathrm{J\,m^{-3}}$, $A = 2 \times 10^{-11}\,\mathrm{J\,m^{-1}}$. As in any Landau-type description of thermodynamics of a phase transition, all energy terms are assumed to have the symmetry of the parent phase; thus, in our simulations, the magnetocrystalline anisotropy coefficients used in the anisotropy energy are related to the austenite. The coefficients in the Landau free energy were obtained by fitting the experimental measurements [35,37]: $Q_1 = 2.32 \times 10^{11}\,\mathrm{J\,m^{-3}}$, $Q_{20} = 3.78 \times 10^8\,\mathrm{J\,m^{-3}}$, $Q_3 = 0.40 \times 10^{10}\,\mathrm{J\,m^{-3}}$, $Q_4 = 7.50 \times 10^{10}\,\mathrm{J\,m^{-3}}$, the magnetoelastic coefficient [37] $B = 4.00 \times 10^6\,\mathrm{J\,m^{-3}}$. For a bulk tetragonal Ni_2MnGa crystal, to avoid solving the mechanical equilibrium equation with inhomogeneous modulus, we chose c_{11} as the average of c_{11} and c_{33}, c_{12} the average of c_{12} and c_{13}, and c_{44} the average of c_{44} and c_{66}: $c_{11} = 1.60 \times 10^{11}\,\mathrm{N\,m^{-2}}$, $c_{12} = 1.52 \times 10^{11}\,\mathrm{N\,m^{-2}}$, and $c_{44} = 0.43 \times 10^{11}\,\mathrm{N\,m^{-2}}$. The original elastic coefficient can be found in [38]. The martensitic transformation temperature of a defect-free crystal is $T_M^0 = 300\,\mathrm{K}$. The time-step for integration is $\Delta t/t_0 = 0.1$, where

$$t_0 = \frac{1+\alpha^2}{\gamma_0 M_s}.$$

The cell size is 18 nm; thus, the system size is around $4.6 \times 4.6\,\mu\mathrm{m}$.

4. Simulation results

The schematic setup of our simulation cell is shown in Figure 1 in an attempt to model experimental conditions [2–8]. Firstly, we obtained an initial domain structure and martensitic microstructure by assigning random orientations for the magnetization and a zero value plus a small random noise for the martensite strain order parameters at 250 K (right side of Figure 1). Then, we increased the magnetic field along the x-axis to saturation and, subsequently, decreased it and finally reverse its

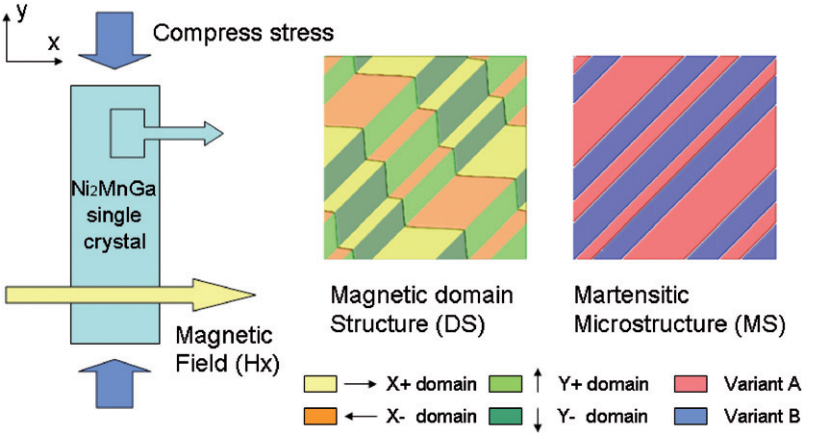

Figure 1. Schematic of the magneto-mechanical setup and the initial domain structure and martensitic microstructure.

direction to saturate magnetization in the opposite direction. During the process, a compressed stress was constantly applied along the y-axis. For every 60 kA m^{-1}, we output the magnetic domain structure and the martensitic microstructure, and also record the magnetization in the x-direction and the strain value in the y-direction to generate the hysteresis loops.

The magnetic field-induced strain curve and the magnetization hysteresis loop under different constant compressive stresses are shown in Figure 2.

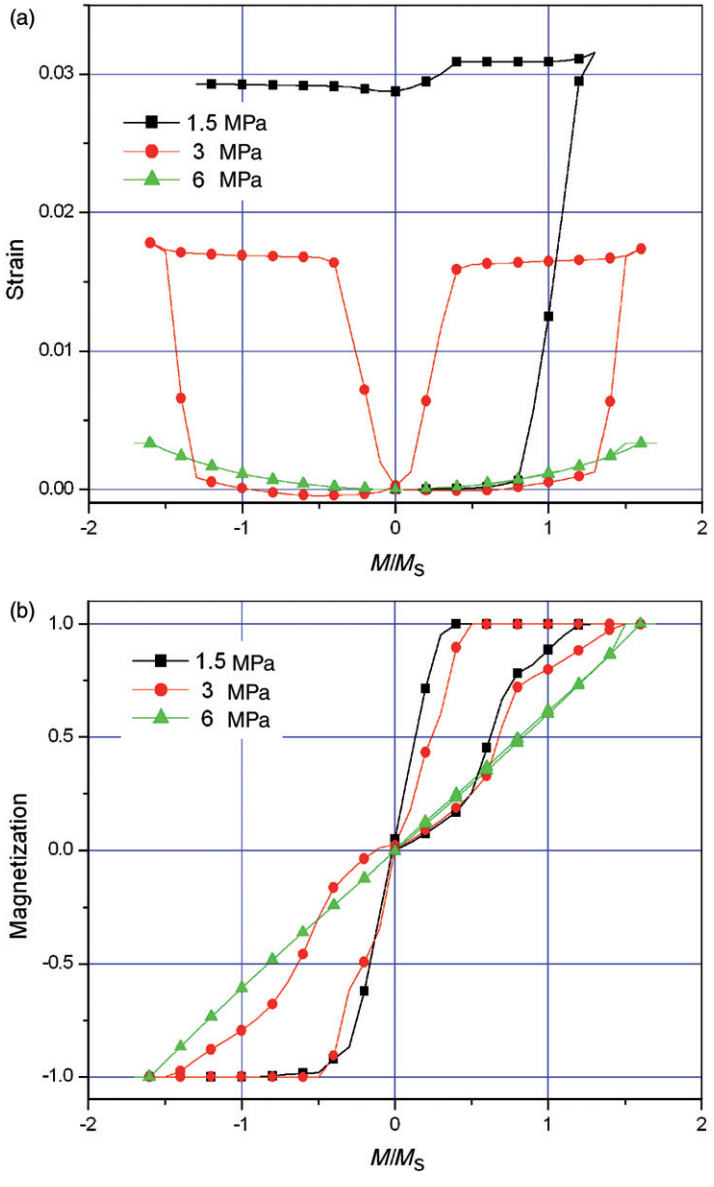

Figure 2. Strain curve (a) and magnetization curve (b) at different compressions.

Three dramatically different types of magnetic field-induced strains are obtained, corresponding to compressive stress levels of 1.5, 3 and 6 MPa, separately. For 1.5 MPa (Case I), when the magnetic field was reduced to zero, the magnetization was recovered with a large hysteresis, whereas the magnetic field-induced strain is not recovered. For case II at 3 MPa, both the magnetization and strain were recovered with a wide hysteresis. For case III (6 MPa), only a small magnetic field-induced strain was obtained, and both the magnetization loop and strain curve exhibit narrow hysteresis.

The magnetic domain and martensitic variant evolution during the magnetization and demagnetization process for case I and case II are shown in Figures 3 and 4, separately. The initial magnetization processes of case I and case II are similar. When a magnetic field is applied perpendicular to the compressive stress direction, the magnetization initially climbs up along a hard-axis. In our phase-field simulation, at a low level of applied magnetic field, we observed that the magnetization vector rotates near the domain wall while there was no significant change in the whole magnetic domain structure. In the next stage, with the increase in applied magnetic field, a jump in magnetization was observed, which can be attributed to the 180° magnetic domain wall motion. It is noted that there was no significant change in

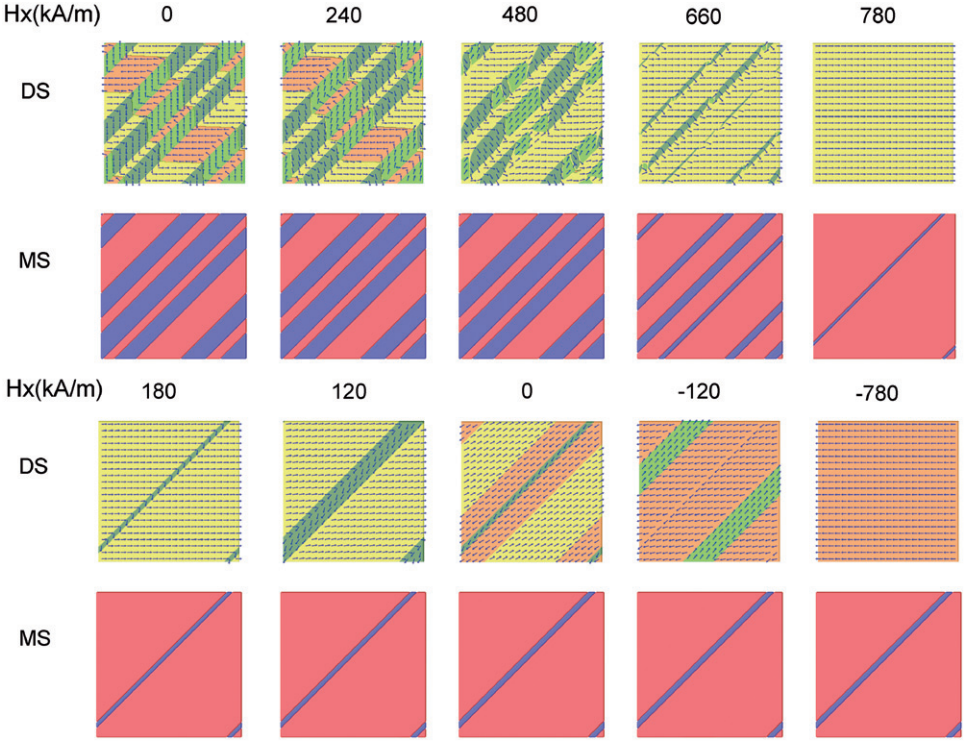

Figure 3. Magnetic domain structure and martensitic microstructure evolution under applied magnetic field at a constant compressive stress of 1.5 MPa. Arrows in domain structure indicate the magnetic vectors.

martensitic microstructures during the first two stages. As the applied magnetic field further increases, the magnetization increases slowly and starts to saturate, whereas the 90° domain wall motion was taking place, leading to the magnetic field-induced strain. After the magnetization reached M_s, different amounts of martensitic variant B was observed for different external compressive stress.

To understand the different MFIS behavior for the three cases, we examine domain structure and martensitic microstructure evolution during switching.

For case I, with the decrease in the applied field, the *y*-magnetic domains first nucleate within the martensite variant B at 180 kA m^{-1}. With a further decrease in the magnetic field, the domain wall motion and magnetization rotation take place simultaneously, as shown in the detailed magnetization vector directions and domain structures in Figure 3. However, the twin boundary is still stationary, i.e. the 90° magnetic domain walls are decoupled from the martensite twin boundary, and, as a result, the strain is not recovered during the removal of the magnetic field.

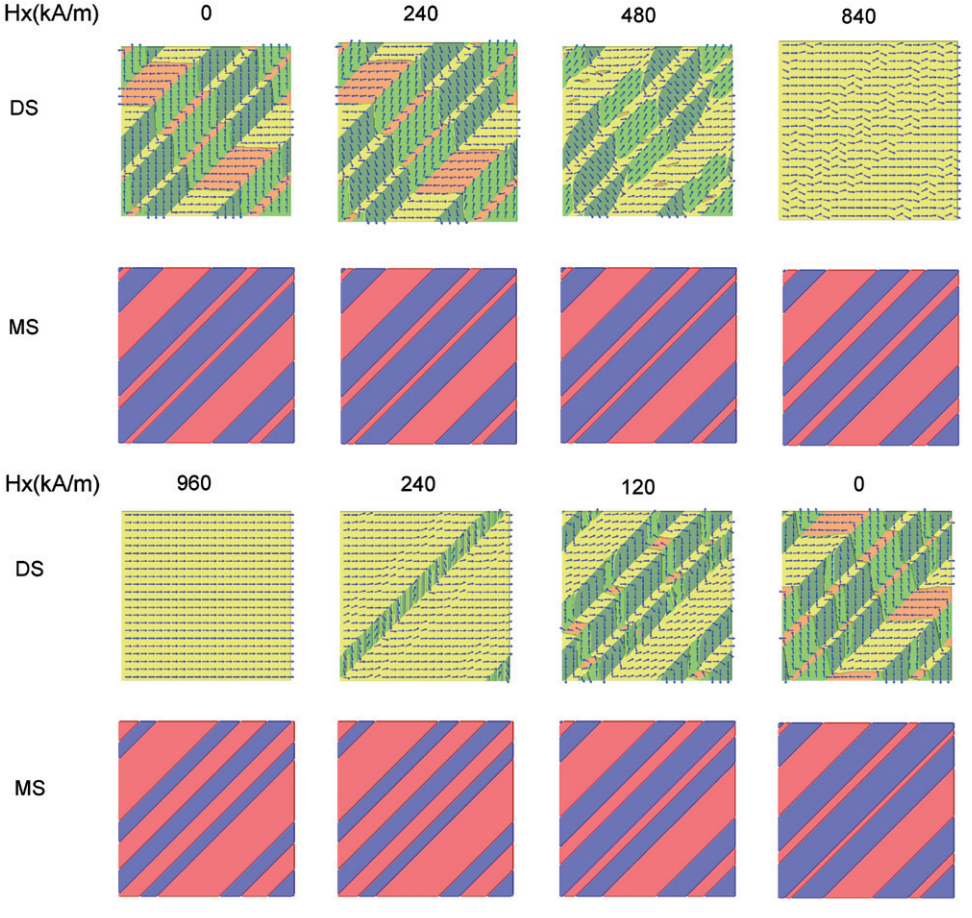

Figure 4. Magnetic domain structure and martensitic microstructure evolution under applied magnetic field at a constant compressive stress of 3 MPa.

When a magnetic field is applied in the opposite direction, the domain walls continue to move with the magnetization along the easy axis. Finally, the magnetization is switched to the $-x$-direction, and the magnetization reaches full saturation (Figure 3). Again, no martensite twin boundary motion is observed in this stage. Subsequent cyclic switching will follow the easy magnetization curves and the procession repeats.

The demagnetization process of Ni_2MnGa under a compression of 3 MPa shows a completely different mechanism, as shown in Figure 4. With a decrease in applied magnetic field, both the magnetization and strain decrease, and return to zero when the magnetic field is completely removed. As the magnetic field decreases, interconnected domains appear in the martensitic variant B at $240\,kA\,m^{-1}$. It was followed by nucleation and growth of x-domains to decrease the demagnetization energy. The appearance of y- and x-domains leads to the reappearance of a stair-case-like domain structure. Meanwhile, 90° magnetic domain wall motion was observed, which results in a decrease in magnetization and also movement of the martensite twin boundaries. Finally, when the magnetic field was completely removed, the domain structure and martensitic microstructure reverted to the initial state, with the magnetization and magnetic field-induced strain decreased to zero.

Once the domain and martensitic structures return to the initial state, the magnetization process in the opposite direction to the magnetic field will be exactly the same as the case discussed above, producing a double loop magnetization curve and butterfly-like strain curve.

The magnetization and strain curves under a larger compressive strain (6 MPa) are shown in Figure 1. The initial state under a 6-MPa stress contains interconnected domains magnetic domain structure and a single variant martensitic microstructure, shown in Figure 5. With the increase in the applied magnetic field, the magnetizations rotate to the hard axis and saturate at large fields while the magnetic domains remain as interconnected. In the demagnetization process, the magnetization rotates back to the initial status due to the compressive stress; the microstructure evolution is demonstrated in Figure 5. Under a compression of 6 MPa, there is no nucleation of second variants during the magnetization process and, as a result, the observed strain is small and purely induced by the elasticity of material itself.

Based on the simulation results above, the entire magnetization and strain hysteresis loops can be understood via the domain/martensite microstructures demonstrated in Figures 3–5. Strain recovery has been actively studied over the last few years [5–8] and a common phenomenon in experiments is the fact that strain did not recover at a low compressive stress but almost fully recover if a larger external compressive stress was applied. Previous studies have attempted to explain strain recovery under a constant compressive stress using schematics or theoretical analysis. On the other hand, our simulations revealed the detailed domain structure evolution, including both the magnetic domain structure and martensite microstructure, which will be invaluable in understanding why and how magnetization and strain changes during the demagnetization process. In our phase field simulations, at a low level of compressive stress, the domain wall motion and magnetization rotation take place simultaneously while the twin boundary is still stationary, as shown in Figure 3, leading to a small strain recovery with a decrease in the magnetic field. As the compressive stress is increased, the nucleation and growth of x-domains was

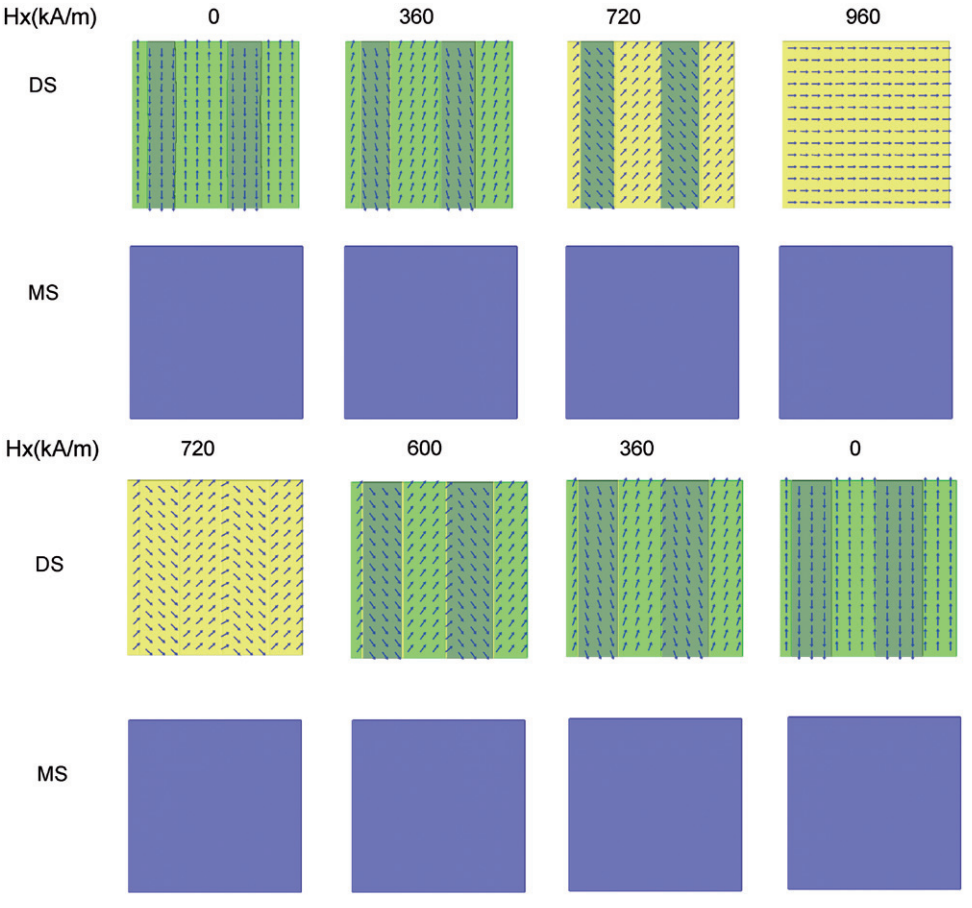

Figure 5. Microstructure evolution under applied magnetic field at a constant compressive stress of 6 MPa. Only magnetization rotation is observed.

observed, and the movement of the 90° magnetic domain wall results in the movement of the martensite twin boundaries, which leads to strain recovery (Figure 4).

Our simulation results can also be used to interpret the first cycle effect discussed in [8]. In the experiment, subjecting the Ni_2MnGa specimen to a cyclic magnetic field loading, it was observed that the MFIS response differed between the first and subsequent magnetic field cycles. In particular, at a low compressive stress, the MFIS showed a high magnitude but it sharply decreased in the second cycle. For case I of our phase-field simulation, the martensite twin boundary moves, accompanying the motion of the 90° magnetic domain walls. However, during the demagnetization process and the subsequent magnetization cycling, magnetic domain wall motion and magnetization rotation take place simultaneously, and thus the 90° magnetic domain walls are decoupled from the martensite twin boundary (Figure 3). At a higher compressive stress, the martensite twin boundary moves during the entire magnetization process and demagnetization process, resulting in the disappearance of the first cycling effect, i.e. case II of our simulations.

In experimental studies, the single variant state is often used as an initial state to reach a high magnetic-induced strain. For comparison, we also performed simulations on switching of a single variant. A compressive stress level of 10 MPa applied along the y-direction ensures an initial single variant state. For each curve, the compression is decreased to the desired stress level and then kept constant. The magnetic field is applied in the x-directions; thus, the magnetization and strain are obtained simultaneously. The magnetization and strain curves for the single variant state are shown in Figures 6a and b, and the detailed magnetic domain and martensitic microstructure evolution are illustrated in Figures 6c and d.

Comparing the simulation results of a single variant with those of a multi-variant system, the two magnetization processes are roughly similar but with some small differences. During the initial magnetization process for the single variant case, the jump in magnetization is due to the movement of the 90° magnetic domain wall associated with martensitic structure reorientation. In the demagnetization process, we also obtained a different recovery strain. At a high compressive stress, interconnected domains were observed in the martensitic variant B, which lead to eventual strain recovery.

The magnetization process under a compressive stress has been previously modeled by a phase-field model [25]. As pointed out by Li et al. [25], their formulation is quite different from the phase-field model employed in the present work [23]. In addition to magnetization, we used the martensitic phase transformation strain as the phase-field order parameter, while Li et al. [25] employed the volume fraction as the order parameter. Furthermore, they emphasized the strain response only with increasing applied magnetic field while the sample was under a compressive stress. On the other hand, our study focused on the entire magnetization and strain hysteresis loops during magnetic field-induced switching under various compressed strains and, in particular, on strain recoveries with unloading the applied magnetic field.

5. Conclusions

The magnetization and strain behavior of Ni_2MnGa under different compressive stresses was studied using the phase-field method. Our simulation results show that there are three types of magnetic field-induced strain mechanisms depending on the magnitude of the applied compressive stress:

(i) At a relatively low stress level ($\sim$1.5 MPa), the 90° magnetic domain walls are decoupled from the martensite twin boundary in the demagnetization process and, hence, the induced magnetization was recovered with a large hysteresis whereas the magnetic field-induced strain was not recovered.

(ii) At an intermediate stress level ($\sim$3 MPa), both the magnetic domain structure and the martensite microstructure reverted to their initial state when the applied field was completely removed. Therefore, both the magnetization and strain were recovered with a wide hysteresis.

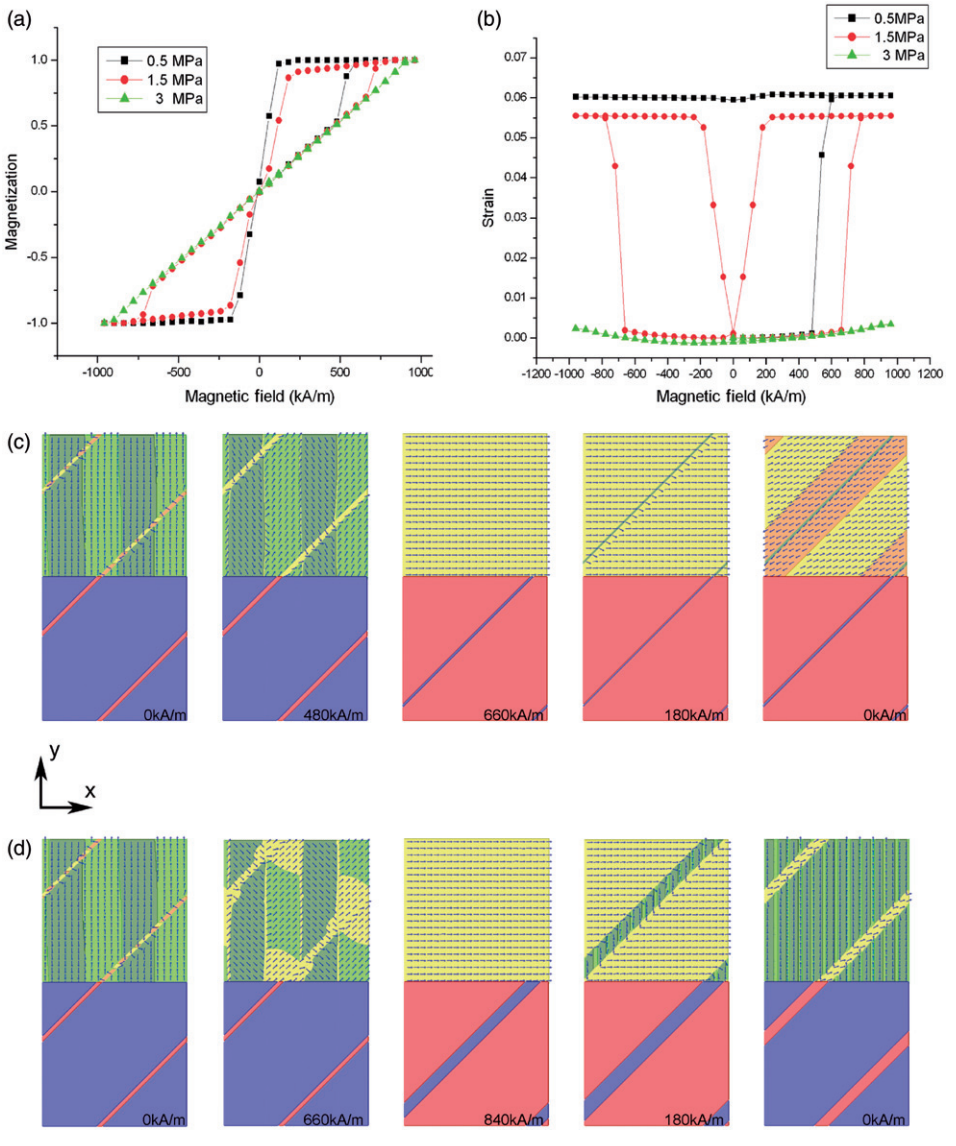

Figure 6. Magnetization curves (a) and strain curves (b) for a single variant simulation. Magnetic vector maps and martensitic microstructure evolution for 0.5 and 1.5 MPa are shown in (c) and (d), respectively.

(iii) At a relatively high stress level (~6 MPa), the martensite microstructure remained as a single variant and only magnetization rotation was observed. A small magnetic field-induced strain was obtained, and both the magnetization loop and strain curve exhibited a narrow hysteresis.

Acknowledgements

This work was supported by the Joint Research Fund for Overseas Chinese Young Scholars from the National Science Foundation of China (50428101) and the US National Science Foundation under the grant number DMR-1006541.

References

[1] K. Ullakko, J.K. Huang, C. Kantner, R.C. O'Handley and T.A. Lograsso, Appl. Phys. Lett. 69 (1996) p.1966.
[2] O. Heczko, N. Lanska, O. Soderberg and K. Ullakko, J. Magn. Magn. Mater. 242/245 (2002) p.1446.
[3] O. Heczko, L. Straka and K. Ullakko, J. Phys. IV 112 (2003) p.959.
[4] P. Müllner, V. Chernenko and G. Kostorz, Scripta Mater. 49 (2003) p.129.
[5] L. Straka and O. Heczko, J. Magn. Magn. Mater. 290/291 (2005) p.829.
[6] O. Heczko, J. Magn. Magn. Mater. 290/291 (2005) p.787.
[7] H.E. Karaca, I. Karaman, B. Basaran, Y.I. Chumlyakov and H.J. Maier, Acta Mater. 54 (2006) p.233.
[8] B. Kiefer, H.E. Karaca, D.C. Lagoudas and I. Karaman, J. Magn. Magn. Mater. 312 (2007) p.164.
[9] G. Li, Y. Liu and B.K.A. Ngoi, Scripta Mater. 53 (2005) p.829.
[10] N. Sarawate and M. Dapino, Appl. Phys. Lett. 88 (2006) p.121923.
[11] N.N. Sarawate and M.J. Dapino, J. Appl. Phys. 101 (2007) p.123522.
[12] R.N. Couch and I. Chopra, Smart Mater. Struct. 16 (2007) p.S11.
[13] A. Sozinov, A.A. Likhachev and K. Ullakko, Proc. SPIE 4333 (2001) p.189.
[14] A. Sozinov, A. Likhachev, N. Lanska and K. Ullakko, Appl. Phys. Lett. 80 (2002) p.1746.
[15] I. Suorsa, J. Tellinen, E. Pagounis, I. Aaltio, and K. Ullakko, in *Proceedings of the Eighth International Conference ACTUATOR 2002*, Bremen, Germany, 10–12 June 2002, H. Borgman, ed., Messe-Bremen, Bremen, 2002, p.158.
[16] J. Tellinen, I. Suorsa, A. Jaaskelainen, I. Aaltio and K. Ullakko, Scripta Mater. 49 (2003) p.566.
[17] D.I. Paul, J. Marquiss and D. Quattrochi, J. Appl. Phys. 93 (2003) p.4561.
[18] D.I. Paul, W. McGehee, R.C. O'Handley and M. Richard, J. Appl. Phys. 101 (2007) p.123917.
[19] V.A. L'vov, E.V. Gomonaj and V.A. Chernenko, J. Phys. Condens. Matter 10 (1998) p.4587.
[20] V.A. Chernenko, V.A. L'vov, P. Müllner, G. Kostorz and T. Takagi, Phys. Rev. B 69 (2004) p.134410.
[21] A.A. Likhachev, A. Sozinov and K. Ullakko, Mech. Mater. 38 (2006) p.551.
[22] T. Koyama and H. Onodera, Mater. Trans. 44 (2003) p.2503.
[23] J.X. Zhang and L.Q. Chen, Phil. Mag. Lett. 85 (2005) p.533.
[24] S. Sreekala and G. Ananthakrishna, Phys. Rev. B 72 (2005) 134403 p.134403.
[25] L.J. Li, J.Y. Li, Y.C. Shu, H.Z. Chen and J.H. Yen, Appl. Phys. Lett. 92 (2008) p.172504.
[26] Y.M. Jin, Appl. Phys. Lett. 94 (2009) p.062508.
[27] Y.M. Jin, Acta Mater. 57 (2009) p.2488.
[28] Y.U. Wang, J. Mater. Sci. 44 (2009) p.5225.
[29] A.N. Vasilev, A.D. Bozhko and V.V. Khovailo, Phys. Rev. B 59 (1999) p.1113.
[30] R.C. O'Handley, *Modern Magnetic Materials: Principles and Applications*, Wiley, New York, 2000.
[31] A.G. Khachaturyan and G.A. Shatalov, Sov. Phys. JETP 29 (1969) p.557.

[32] A.G. Khachaturyan, *Theory of Structural Transformations in Solids*, Wiley, New York, 1983.
[33] X.P. Wang and C.J. Garcia-Cervera, J. Comp. Phys. 171 (2001) p.357.
[34] L.Q. Chen and J. Shen, Comput. Phys. Commun. 108 (1998) p.147.
[35] R. Tickle and R.D. James, J. Magn. Magn. Mater. 195 (1999) p.627.
[36] D.I. Paul, J. Marquiss and D. Quattrochi, J. Appl. Phys. 93 (2003) p.4561.
[37] N. Glavatska, G. Mogilniy and I. Glavatsky, J. Phys. IV 112 (2003) p.963.
[38] L. Dai, J. Cullen and J. Cui, Mater. Res. Soc. Symp. Proc. 785 (2004) p.D2.2.